JOURNAL OF Applied Polymer SCIENCE

Enhancement of dielectric constants of epoxy thermosets via a fine dispersion of barium titanate nanoparticles

Lei Li, Sixun Zheng
Department of Polymer Science and Engineering and State Key Laboratory of Metal Matrix Composites, Shanghai Jiao Tong University, Shanghai 200240, People's Republic of China
Correspondence to: S. Zheng (E-mail: szheng@sjtu.edu.cn)

ABSTRACT: In this study, we examined a facile approach for achieving a fine dispersion of barium titanate (BT) nanoparticles (NPs) in epoxy thermosets. First, the surfaces of BT NPs were modified with poly(ε-caprolactone) (PCL) via a surface-initiated ring-opening polymerization approach. We found that the PCL-grafted BT NPs were easily dispersed in epoxy thermosets. The fine dispersion of the PCL-grafted BT NPs in the epoxy thermosets was evidenced by transmission electron microscopy and dynamic mechanical thermal analysis. We found that the organic–inorganic nanocomposites displayed significantly enhanced dielectric constants and low dielectric loss compared to the control epoxy. The nanocomposites containing 14.1 wt % BT NPs possessed dielectric constants as high as at a frequency of 10^3 Hz. The dielectric loss was measured to be 0.002 at a frequency of 10^3 Hz. The improved dielectric properties are accounted for the fine dispersion of the BT NPs in the epoxy thermosets. © 2015 Wiley Periodicals, Inc. J. Appl. Polym. Sci. **2016**, *133*, 43322.

KEYWORDS: composites; dielectric properties; nanostructured polymers; thermosets

Received 6 July 2015; accepted 8 December 2015
DOI: 10.1002/app.43322

INTRODUCTION

Epoxies are a class of important thermosetting polymers; they are extensively applied as the matrix of composites and adhesives because of their excellent mechanical properties and high chemical resistance.[1–4] Epoxies have been also used as electric encapsulation materials for embedded passives, such as resistors, capacitors, and inductors, because of their mechanical properties, low-temperature processability, and compatibility with integrated circuit boards.[5,6] Depending on the different requirements in dielectric applications, insulating materials (e.g., epoxy) can be designed to display various dielectric properties. For high-speed digital circuits with a high frequency, epoxies are required to possess a low dielectric constant; this is favorable for the miniaturization and integration of the devices.[7] To facilitate the electric charge storage, transportation, and heat dissipation, nonetheless, epoxy polymers with improved dielectric constants are highly desirable.[8,9] It is important to modulate the dielectric properties of epoxy materials to meet various requirements.

Organic–inorganic epoxy nanocomposites with high dielectric constants have attracted considerable interest in the microelectronics industry because of their easy processing, compatibility with printed wiring boards, and low cost.[10–18] It has been realized that the dielectric constant of epoxies can be increased through the incorporation of conductive fillers (e.g., carbon nanotubes,[19–21] metals,[22,23] conductive polymers[24,25] or high-electric-constant ceramic fillers, such as ZrO_2,[26] TiO_2,[27–29] and $BaTiO_3$.[30–39] Epoxy composites filled with conductive fillers can exhibit high dielectric constants; however, this class of composites can suffer from a very high dielectric loss because of the high electrical conductivity of the fillers. This greatly limits applications of the composite materials in the electric industry. In marked contrast to composites containing conductive fillers, composites containing nanosized ceramics with high dielectric constants can display quite high dielectric constants but relatively low dielectric losses.[26–39] Barium titanate (BT) is a traditional ferroelectric ceramic, and it has excellent dielectric properties: a high dielectric constant and a low dielectric loss. The excellent dielectric properties of BT mainly result from its capability to spontaneously polarize.[40,41] At room temperature (below the Curie point), the structure of BT ceramic changes; the center Ti^{4+} ion shifts by a small distance away from the center and toward the O^{2-} ion along the stretched axis. The loss in balance between the positive and negative electric charges results in polarization. The excellent dielectric properties of BT have inspired the preparation of nanocomposites containing BT nanoparticles (NPs) to improve the dielectric properties of epoxy thermosets. In addition, to the breakdown strengths, it has been realized that types, sizes, and dispersion degrees of inorganic fillers are important factors that influence the dielectric properties of organic–inorganic composites. However, simple physical mixing

would cause undesired aggregation of the inorganic NPs because of the inherent incompatibility between the organic and inorganic components; this significantly limits the enhancement of the dielectric properties of the composites. For a successful application, measures must be taken to suppress the macroscopic aggregation of the inorganic fillers in organic polymers. In past years, there have been some reports on the preparation of organic–inorganic nanocomposites of epoxy thermosets with BT NPs in epoxy thermosets.[30–37] Alam *et al.*[31] reported the utilization of some dispersants, such as phosphate esters, to improve the dispersion of BT NPs in BT/epoxy nanocomposites. However, the incorporation of these highly polar dispersants could result in an increase in the leakage current and the dielectric loss.[32] Recently, the surface chemical modification of BT NPs was applied to improve the dispersion of BT NPs in epoxy thermosets. Of the various approaches used for surface modification, organosilane coupling agents bearing the functional groups reactive with epoxy (e.g., epoxide and amino groups) were often used. We found that the formation of the chemical linkages between the epoxy and BT NPs were critical in the suppression of the aggregation of the inorganic components in the organic matrix.[33–38] For instance, Iijima *et al.*[33] modified the surface of BT NPs with 3-glycidoxypropyl trimethoxysilane and achieved a fine dispersion of BT NPs in the epoxy matrix via the interfacial reaction of BT NPs with the epoxy matrix. Huang *et al.*[37] reported the surface modification of BT NPs with organosilane coupling agents bearing some reactive groups, such as epoxide, thiol, and amino groups. They investigated the effect of surface modification on the processing, energy storage, and breakdown strength of BT/epoxy composites. With the previous approaches, some associated techniques, such as sonication ultrasonic agitation, stirring with high rotation, and revolution speed, were still required to disperse the inorganic NPs[33,37] in the organic matrix because there were competitive kinetics between the dispersion of the inorganic NPs and the reaction of the reactive NPs with the matrix.

In this article, we report an approach for improving the dispersion of BT NPs via a simple physical blending approach. Toward this end, we first explored the preparation of the BT NPs, the surfaces of which were functionalized with poly(ε-caprolactone) (PCL). The PCL-grafted BT NPs were prepared via surface-initiated ring-opening polymerization (ROP). It was expected that the PCL chains would stabilize the dispersion of the BT NPs until the sufficiently higher conversion of epoxy because PCL is miscible with epoxy after and before curing reactions.[42,43] The modified BT NPs were characterized by Fourier transform infrared (FTIR) spectroscopy, thermogravimetric analysis (TGA), X-ray photoelectron spectroscopy (XPS), wide-angle X-ray diffraction, differential scanning calorimetry (DSC), transmission electron microscopy (TEM), and dynamic mechanical thermal analysis (DMTA). Thereafter, the dielectric properties were examined with broadband dielectric spectroscopy.

EXPERIMENTAL

Materials

Diglycidyl ether of bisphenol A (DGEBA) was purchased from Shanghai Resin Co. (China). It had a quoted epoxide equivalence of 185–210. 4,4′-Methylene bis(2-chloroaniline) (MOCA) was used as the hardener; it was purchased from Shanghai Reagent Co. (China). ε-Caprolactone (CL: 99%) was purchased from Acros Co. (Shanghai, China). Before use, CL was distilled over calcium hydride (CaH_2) under reduced pressure. 3-Aminopropyltriethoxysilane (APTES) was purchased from TCI Co. (Shanghai, China) and was used as received. BT NPs were purchased from Aladdin Co. (Shanghai, China). Stannous octanoate [$Sn(Oct)_2$] was purchased from Aldrich Co. (Shanghai, China). Other organic solvents were purchased from Shanghai Reagent Co. (China). Before use, toluene was refluxed over sodium and then distilled.

Surface Modification of the BT NPs

First, the surface of the plain BT NPs was treated with hydrogen peroxide (H_2O_2) to generate more hydroxyl groups. To a flask equipped with a magnetic stirrer, the BT NPs (5.00 g) and an aqueous solution of H_2O_2 (30 wt %, 80 mL) were charged with vigorous stirring. The mixture was ultrasonically irradiated for 30 min and was then refluxed at 106°C for 6 h. After it was cooled to room temperature, the mixture was centrifuged to obtain the solids. The solids were then washed with deionized water three times. After they were dried *in vacuo* at 40°C for 12 h, the surface-modified BT (denoted BT–OH) NPs (4.84 g) were obtained at a yield of 96.8%.

FTIR spectroscopy (cm^{-1}, KBr window): 3510 and 3422 (O—H), 570 (Ti—O).

Second, the surfaces of BT–OH NPs were further treated with APTES with a method found in the literature.[44] Typically, the BT–OH NPs (2.00 g) were dispersed into anhydrous toluene (120 mL), and then, APTES (5.00 g) was added. The mixture was heated to 80°C and maintained at this temperature for 24 h with vigorous stirring. The BT NPs were isolated with a centrifuge and were then washed with deionized water three times. After it was dried *in vacuo* at 80°C for 12 h, the product (denoted BT–NH_2 NPs; 1.92 g) was obtained at a yield of 93.1%.

FTIR spectroscopy (cm^{-1}, KBr window): 3510 (O—H), 3390 (N—H), 2900 (C—H), 1575 (N—H), 1113 (Si—O—Ti), 1034 (Si—O—Si), 570 (Ti—O).

Surface-Initiated ROP

To a flask equipped with a magnetic stirrer, the previous BT–NH_2 NPs (1.50 g), CL (3.00 g, 26.3 mmol), and anhydrous toluene (9 mL) were charged. The flask was connected to a Schlenk line to degas via three pump–freeze–thaw cycles, and then, $Sn(Oct)_2$ (10.65 mg, 0.0263 mmol) was added and used as a catalyst with vigorous stirring. The polymerization was performed at 100°C for 24 h. The polymerized product was dispersed in chloroform. With centrifugation, the surface-grafted BT NPs were obtained. The crude product was redispersed with chloroform and then collected with centrifugation. This procedure was repeated three times to purify the product. After it was dried *in vacuo* at 30°C for 24 h, the product (3.22 g; denoted as BT-*g*-PCL) was obtained with a conversion of CL of 71.6%.

FTIR spectroscopy (cm^{-1}, KBr window): 3510 (O—H), 2900 (C—H), 1725 (—COO—), 1575 (N—H), 1113 (Si—O—Ti), 1034 (Si—O—Si), 570 (Ti—O).

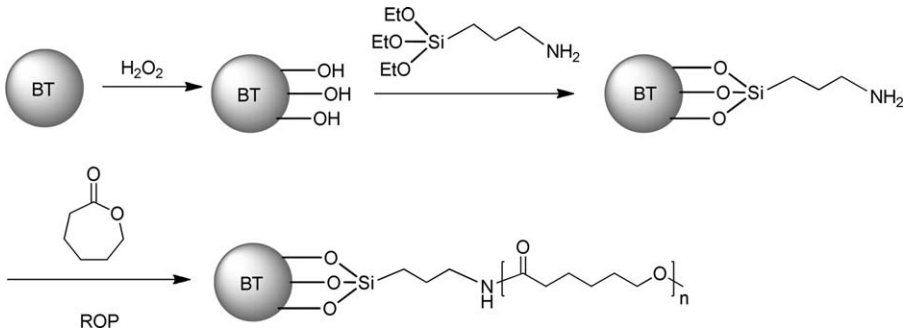

Scheme 1. Synthesis of the PCL-grafted BT NPs.

Preparation of the Nanocomposites

A desired amount of the BT-*g*-PCL NPs was added to the preweighted DGEBA with vigorous stirring, and an equimolar amount of MOCA with respect of the epoxide groups of the DGEBA was added with continuous stirring until the curing agent was fully dissolved. The mixture was poured into Teflon molds and cured at 150°C for 3 h and then at 180°C for 2 h. In this study, the weight ratios of the BT-*g*-PCL NPs and DGEBA were 1:9, 2:8, 3:7, and 4:6 (these samples are denoted as BT/EP1, BT/EP2, BT/EP3, and BT/EP4, respectively).

Measurement and Techniques

FTIR Spectroscopy. FTIR spectroscopy was performed on a PerkinElmer Paragon 1000 Fourier transform spectrometer at room temperature. Before the measurements, the samples were granulated and then mixed with KBr pellets. The mixtures were pressed into small flakes and subjected to FTIR measurements. In all of the measurements, the spectra were recorded with 64 scans at a resolution of 2 cm^{-1}.

TGA. TGA measurements were carried out on a TA Instruments Q5000 thermogravimetric analyzer. The measurements were performed in an air flow (50 mL/min) from 40 to 800°C at a heating rate of 20°C/min. The temperature at which a 5 wt % weight loss occurred was taken as the initial degradation temperature.

TEM. Morphological observation was performed on a JEOL JEM-2010 high-resolution transmission electron microscope at an acceleration voltage of 200 kV. For the BT and BT-*g*-PCL NPs, the samples were first dispersed in ethanol, and the suspensions were dropped onto 300-mesh copper grids. The solvent was slowly evaporated at room temperature to remove the majority of the solvent, and the residual solvent was eliminated by drying the sample *in vacuo* at 40°C for 10 h. For the thermosetting nanocomposites containing BT-*g*-PCL NPs, the samples were trimmed into slices with a thickness of approximately 70 nm. The sections were placed on 300-mesh copper grids for observation.

Wide-Angle X-ray Diffraction. Wide-angle X-ray diffraction experiments were carried out on a D/max-2200/PC diffractometer with Cu Kα ($\lambda = 0.154$ nm) irradiation at 40 kV and 30 mA with a Ni filter. Data were recorded in the range $2\theta = 5$–80° at a scanning rate of 4.0 °/min and a step size of 0.02°, respectively.

XPS. XPS spectra were recorded with an AXIS Ultra DLD photoelectron spectrometer with monochromatic Al Kα. Survey scans were carried out over a binding energy range of 0–1200 eV with a constant detector pass energy range of 0–160 eV. Data were treated with XPS PEAK version 4.1 software.

DSC. Calorimetric measurements were performed on a PerkinElmer Pyris-1 differential scanning calorimeter. The instrument was calibrated with an indium standard, and the measurements were conducted in a nitrogen flow (50 mL/min). The samples were first heated to 200°C and held at this temperature for 3 min to remove the thermal history. Thereafter, the samples were quenched to −80°C. The second heating scan with a heating rate of 20°C/min was recorded as the heating thermogram. The midpoint of the heat capacity change and the maximum endothermic transition were taken as the glass-transition temperature and melting temperature (T_m), respectively.

DMTA. Dynamic mechanical measurements were carried out on a TA Instruments DMA Q800 dynamic mechanical thermal analyzer. The tests were operated in single-cantilever mode, and the frequency was 1.0 Hz. DMTA measurements were performed from −100 to 200°C at a heating rate of 3.0°C/min.

Dielectric Constant Measurement. The broadband frequency dielectric properties were measured on a Solartron SI 1260 impedance analyzer (Advanced Measurement Technology, Inc., United Kingdom) in the frequency range 10^2–10^7 Hz at room temperature. Disklike specimens with a diameter of 1.0 cm and a thickness of 3.5 mm were prepared. Before the measurements, each of the two surfaces of the specimen was sputtered with a layer of gold (~0.1 μm in thickness) as the electrodes.

RESULTS AND DISCUSSION

Surface Functionalization of BT NPs

The route of preparation for the BT-*g*-PCL NPs is depicted in Scheme 1. First, the surfaces of the BT NPs were activated to generate hydroxyl groups through refluxing in H_2O_2 aqueous solution. Second, the surface-activated BT NPs (denoted as BT–OH NPs) were further treated with APTES to obtain 3-aminopropyl-functionalized BT NPs (denoted as BT–NH_2 NPs). The amino groups at the surfaces of the BT NPs were used as the initiating sites for the ROP of CL, and the PCL-grafted BT NPs (denoted as BT-*g*-PCL NPs) were thus obtained. Shown in Figure 1 are the FTIR spectra of the BT–OH, BT–NH_2, and BT-*g*-PCL NPs. For the BT–OH NPs, the shoulder band at 3510 cm^{-1} was assignable to the free hydroxyl groups, whereas the broad band centered at 3422 cm^{-1} was attributable to the stretching vibrations of the

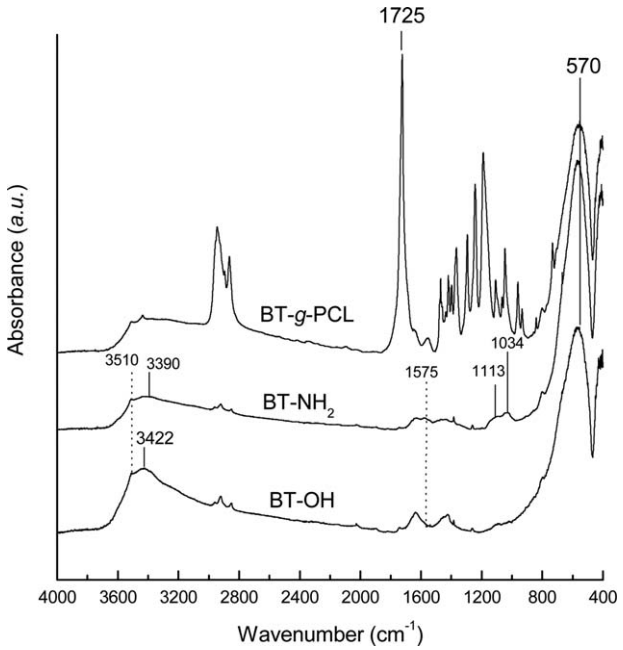

Figure 1. FTIR spectra of BT–OH, BT–NH_2, and BT-*g*-PCL NPs.

hydroxyl groups at the surfaces of the BT NPs. The intense band at 570 cm^{-1} was characteristic of the stretching vibrations of Ti—O bonds.[45] A few bands at 2910, 1632, and 1426 cm^{-1} could result from the residues of the organic precursor of the BT NPs.[46] After the surfaces of the BT NPs were treated with APTES, new bands appeared at 1034, 1113, and 1575 cm^{-1}. The first two were assigned to the stretching vibrations of Si—O—Si and Si—O—Ti linkages, whereas the last band was assigned to the deformation vibrations of the N—H bond of the amino group. Notably, the band at 3422 cm^{-1} of the BT–OH NPs became broader and shifted to 3390 cm^{-1}. This indicates the occurrence of a surface reaction between the BT NPs and APTES; that is, the surfaces of the BT–OH NPs were functionalized with 3-aminopropyl groups. There were still some free hydroxyl groups at the surfaces of the APTES-functionalized BT NPs because the stretching vibration band of free hydroxyl groups at 3510 cm^{-1} was also found in the BT–NH_2 NPs. Nonetheless, FTIR spectroscopy indicates that the surfaces of the BT–OH NPs were successfully functionalized with APTES.

XPS was carried out to measure the surface elemental content of the modified BT NPs. The XPS spectra of the BT–OH, BT–NH_2, and BT-*g*-PCL NPs are shown in Figure 2. Four main binding energy signals were exhibited; these corresponded to Ba 3d5 (778 eV), Ti 2p3 (458 eV), O1s (530 eV), and C1s (287.5 eV).[47] After treatment with APTES, two new peaks appeared at 102 and 399 eV, which were due to Si 2p and N1s, respectively. This observation indicates that the surfaces of the BT NPs were successfully functionalized with APTES. For the BT-*g*-PCL NPs, the content of surface elemental carbon was measured to be 77%; this was higher than that of the BT–NH_2 NPs (64%). The increase in the surface elemental carbon content indicates that the PCL chains were grafted onto the surface of the BT NPs.

The BT–OH and BT–NH_2 NPs were subjected to TGA, and the TGA curves are shown in Figure 3. For the BT–OH NPs, a degradation step occurred at about 390°C; this could result from the release of water because of the condensation of surface hydroxyl groups of the NPs.[39] For the BT–NH_2 NPs, a similar TGA profile was displayed, but the yield of residue at 800°C (96.5%) was slightly lower than that of BT–OH NPs at 800°C (97.4%). The decreased residue yield was attributable to the decomposition of the organic portion from the 3-aminopropyl moieties of the BT–NH_2 NPs. According to the slight difference in the degradation yields, the content of 3-aminopropyl groups at the surface of the BT–NH_2 NPs (C) was estimated to be 0.091 mmol/g. With the 3-aminopropyl groups at the surfaces of the BT–NH_2 NPs, the surface-initiated ROP of CL was carried out to afford PCL-grafted BT NPs (denoted as BT-*g*-PCL NPs). Also shown in Figure 1 is the FTIR spectrum of the BT-*g*-PCL NPs. The intense bands centered at about 2900 cm^{-1} were attributable to the stretching vibrations of the C—H bonds from the methylene groups of the aliphatic PCL chains. The band at 1725 cm^{-1} was assigned to the stretching vibrations of the carbonyl groups of the PCL chains. The band at 570 cm^{-1} was assigned to the Ti—O bonds of the BT NPs. The results of FTIR spectroscopy indicate that the product combined the structural features from the PCL and BT NPs; that is, the PCL chains were successfully grafted onto the surfaces of the BT NPs. Also shown in Figure 3 is the TGA curve of the BT-*g*-PCL NPs. The BT-*g*-PCL NPs displayed an initial degradation at about 302°C, and the yield of degradation residue at 800°C was measured to be 42.8%. According to the content of surface 3-aminopropyl groups (0.091 mmol/g) and the yield of degradation residue, the average lengths of PCL chains grafted onto the surfaces of the BT NPs (L) were estimated to be 5900 Da with the following equation:

$$L=(W_1-W_2)/C \quad (1)$$

where W_1 and W_2 are the yields of the residues of the BT–NH_2 and BT-*g*-PCL NPs, respectively, at 800°C.

The structures of the crystals for the plain BT NPs, BT–NH_2, and BT-*g*-PCL NPs were readily investigated by means of wide-

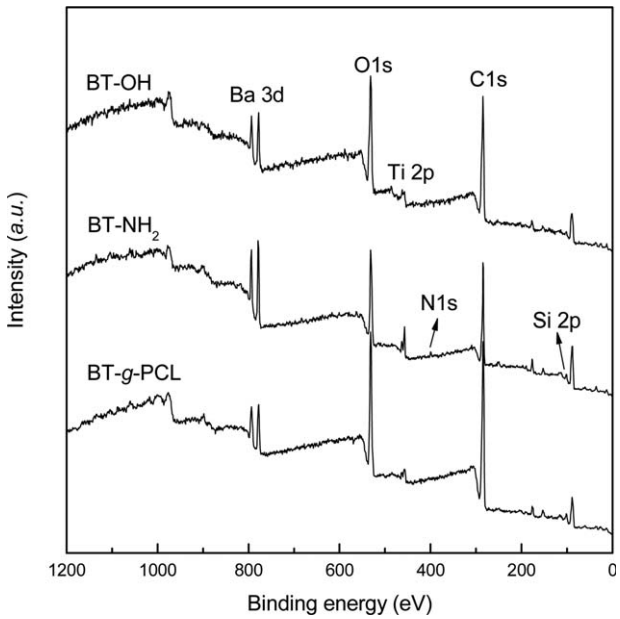

Figure 2. XPS spectra of BT–OH, BT–NH_2, and BT-*g*-PCL NPs.

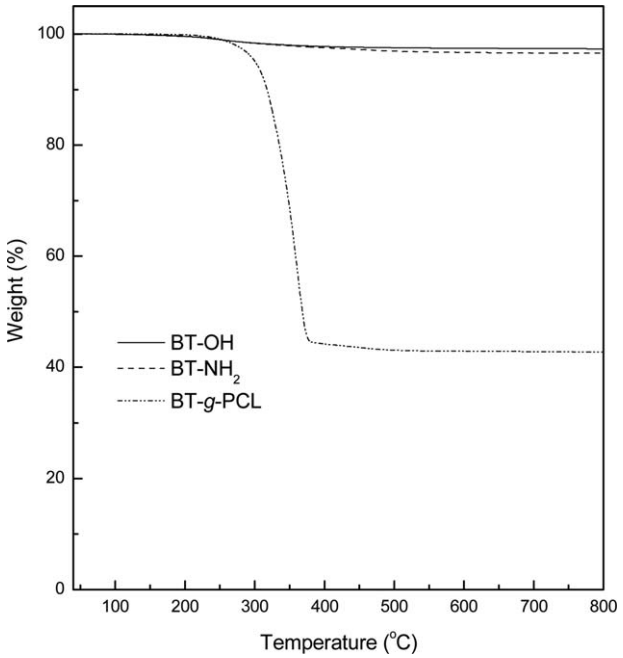

Figure 3. TGA curves of BT–OH, BT–NH_2, and BT-*g*-PCL NPs.

angle X-ray diffraction, and the X-ray diffraction curves are shown in Figure 4. For the plain BT–OH NPs, several intense diffraction peaks were exhibited at 2θ values of 22.0, 31.5, 38.7, 44.8, 50.7, 56.1, 65.5, and 74.5°; these corresponded to the typical (100), (110), (111), (200), (201), (211), (220), and (310) reflections, respectively. The positions of the diffraction peaks were in good agreement with the standard BT NP diffraction data.[48] The BT–NH_2 NPs displayed almost the same diffraction

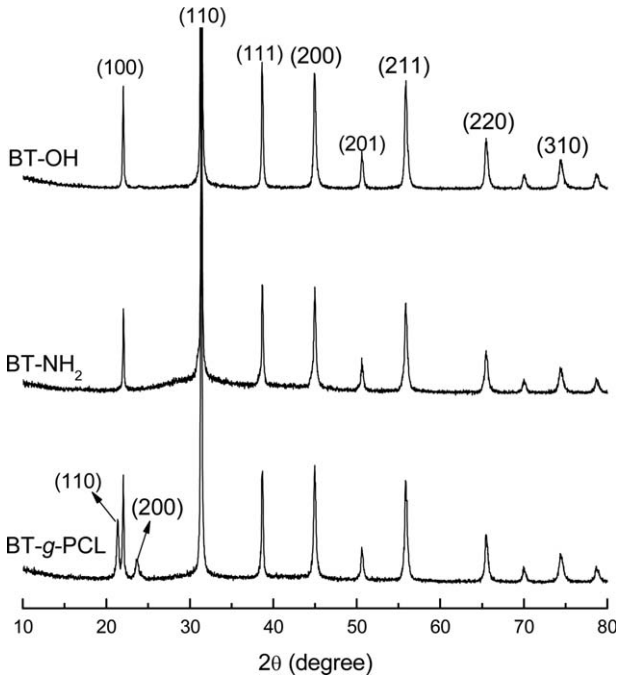

Figure 4. X-ray diffraction curves of BT–OH, BT–NH_2, and BT-*g*-PCL NPs.

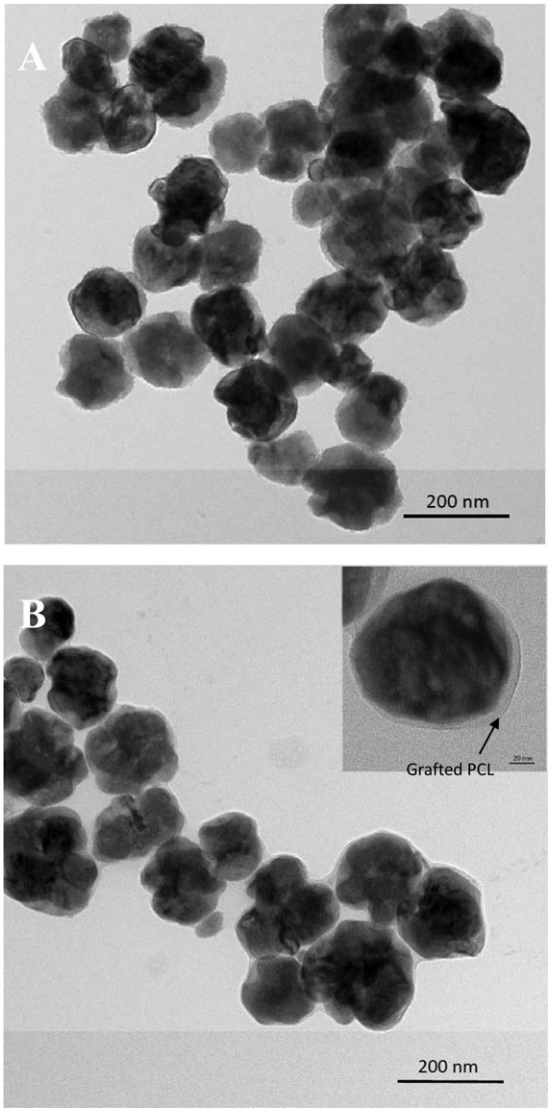

Figure 5. TEM images of the (A) BT–OH and (B) BT-*g*-PCL NPs.

peaks as the plain BT NPs. For the BT-*g*-PCL NPs, new diffraction peaks appeared at 2θs of 21.4 and 23.6° in addition to those assigned to the BT NPs. These diffraction peak positions agreed well with the values reported in the literature with the (110) and (200) reflections of PCL.[49] The results of the previous FTIR spectroscopy, TGA, and X-ray diffraction indicated that PCL-grafted BT NPs were successfully obtained. The morphologies of the BT NPs after and before the surface-grafting polymerization were investigated by means of high-resolution transmission electron microscopy (HRTEM). Shown in Figure 5(A,B) are the TEM micrographs of the unmodified and BT-*g*-PCL NPs. We found that the spherical BT NPs had diameters of 50–100 nm. For the BT-*g*-PCL NPs, the TEM image with the higher magnification [see inset in Figure 5(B)] showed that a layer with a thickness of 4–5 nm was discernable around the surface of the BT NPs. This layer was attributable to the PCL chains grafted onto the surfaces. The PCL chains grafted onto the surfaces of the BT NPs were important for the dispersion of the BT NPs in epoxy thermosets.

Table I. Composition and Thermal Properties of the Epoxy Nanocomposites Containing BT-*g*-PCL NPs

Sample	BT-*g*-PCL/DGEBA	BT NPs (wt %)	T_g	T_d	Residue (%)[a]
Epoxy	—	0	159.0	405.2	0
BT/EP1	1:9	3.20	144.6	379.6	4.30
BT/EP2	2:8	6.40	121.5	365.8	8.40
BT/EP3	3:7	10.3	110.7	350.4	13.7
BT/EP4	4:6	14.1	81.5	350.1	20.1
BT-*g*-PCL NPs	—	42.8	—	300.2	42.8

T_d, temperature at which 5 wt % mass loss occurred according to TGA; T_g, glass-transition temperature measured by DMTA.
[a] The values were taken at 800°C from TGA measurements.

Formation of the Nanocomposites

The above BT-*g*-PCL NPs were incorporated into epoxy to prepare the composites. The compositions of the composites are summarized in Table I. The morphology of the composites was investigated by means of HRTEM. Shown in Figure 6 are the TEM micrographs of the nanocomposites with different contents of BT-*g*-PCL NPs. All of the composites displayed microphase-separated structures, and microdomains with sizes of 100–150 nm were homogeneously dispersed into the continuous matrix. In terms of the difference in the electron densities between the epoxy and BT NPs, we judged that the dark domains were attributable to the BT NPs, whereas the light continuous matrix to epoxy could be mixed with the PCL chains grafted onto the surface of the BT NPs (see Scheme 2). We observed that NPs with sizes of 50–100 nm were dispersed in the continuous epoxy matrices. Notably, the quantity of BT NPs increased with increasing content of BT-*g*-PCL NPs [see Figure 6(A–D)], and no significant aggregation occurred. The results of TEM indicate that the nanocomposites were successfully obtained.

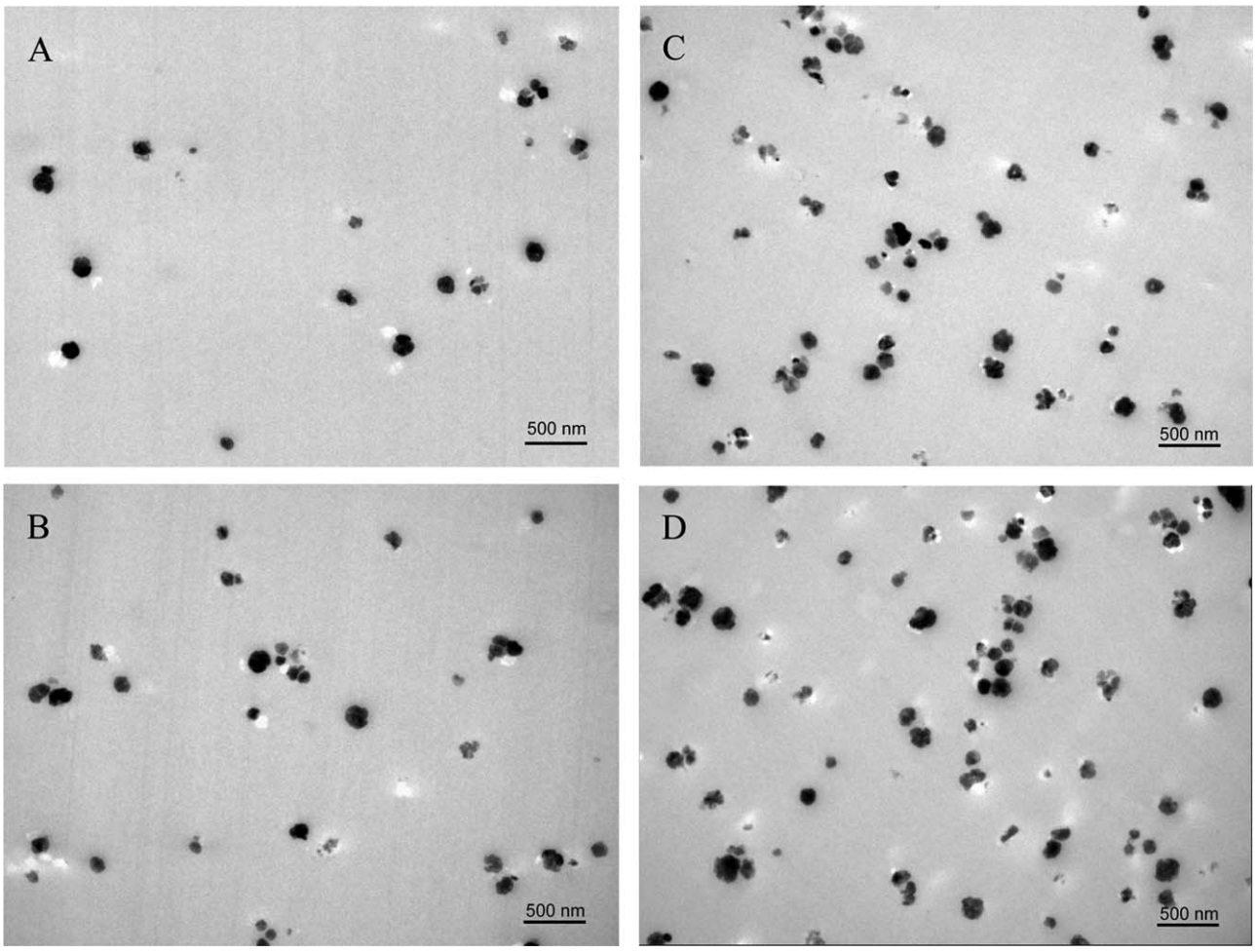

Figure 6. TEM images of the nanocomposites: (A) BT/EP1, (B) BT/EP2, (C) BT/EP3, and (D) BT/EP4.

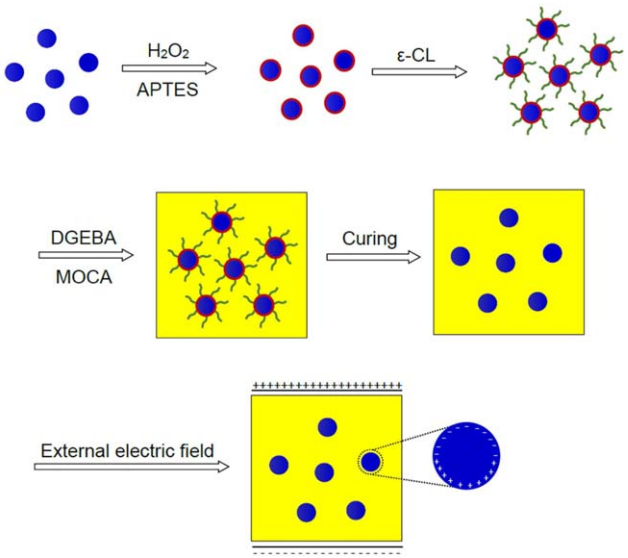

Scheme 2. Formation of the BT nanophases in the epoxy thermosets and polarization of the nanocomposites under an external electric field. [Color figure can be viewed in the online issue, which is available at wileyonlinelibrary.com.]

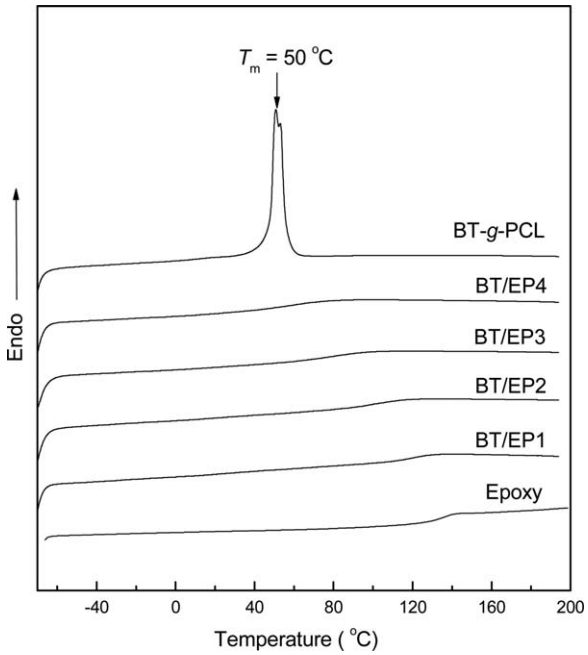

Figure 7. DSC curves of nanocomposites containing epoxy resins and different amounts of BT-*g*-PCL NPs.

The fine dispersion of the BT NPs in the epoxy matrices was attributable to the grafting of PCL chains onto the surface of the NPs. The miscibility of the PCL chains with the epoxy networks stabilized the dispersion of the inorganic NPs in the organic matrices and, thus, suppressed the occurrence of aggregation. To demonstrate the miscibility of the PCL chains of the PCL-grafted BT NPs with the epoxy matrix, the nanocomposites were subjected to DSC, and the DSC curves are shown in Figure 7. For comparison, the DSC curve of the BT-*g*-PCL NPs is also included. For the BT-*g*-PCL NPs, an endothermic peak was observed at 50°C; it was attributed to the melting transition of the PCL in the BT-*g*-PCL NPs. When the BT-*g*-PCL NPs were incorporated into epoxy, the melting peak of PCL disappeared. This observation suggest that the PCL chains were no longer crystallizable in the nanocomposites. We propose that the PCL chains grafted onto the surfaces of the BT NPs were mixed with the epoxy networks on the segmental level (i.e., the PCL chains were miscible with epoxy resins) and their crystallization was thus suppressed. The miscibility of the PCL chains with the epoxy network were evidenced by the glass-transition behavior of the epoxy matrices. For the control epoxy, the glass-transition temperature was measured to be 137°C. Notably, the nanocomposites displayed glass-transition temperatures that were lower than that of the control epoxy, and the glass-transition temperatures of the nanocomposites decreased with increasing content of BT-*g*-PCL NPs (Figure 7). The decreased glass-transition temperatures were responsible for the plasticization of the PCL chain (which possessed glass-transition temperatures as low as −65°C) on the epoxy matrices. The glass-transition behavior was further investigated by means of DMTA. The control epoxy and the nanocomposites were subjected to DMTA measurements, and the DMTA curves are shown in Figure 8. For the control epoxy, the α transition was detected at 159°C; it was assigned to the glass-to-rubber transition of this crosslinked polymer. In addition, the control epoxy displayed a secondary transition (β relaxation) at about −56°C. The secondary transition was predominantly attributable to the hydroxyether structural units in the aromatic amine-crosslinked epoxy.[50] With the addition of BT-*g*-PCL NPs to the epoxy, the α transitions were observed to shift to lower temperatures; that is, the glass-transition temperatures of nanocomposites decreased with increasing content of the BT-*g*-PCL NPs. This result was in

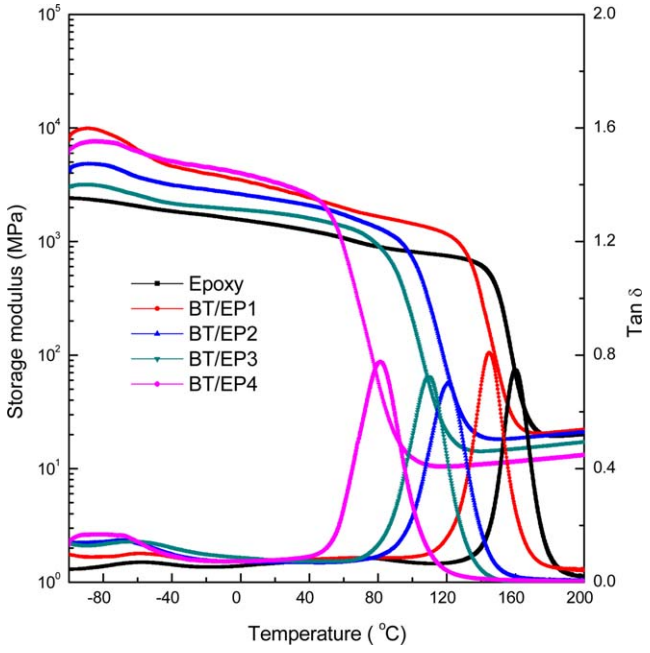

Figure 8. DMTA curves of nanocomposites containing epoxy resins and different amounts of BT-*g*-PCL NPs. [Color figure can be viewed in the online issue, which is available at wileyonlinelibrary.com.]

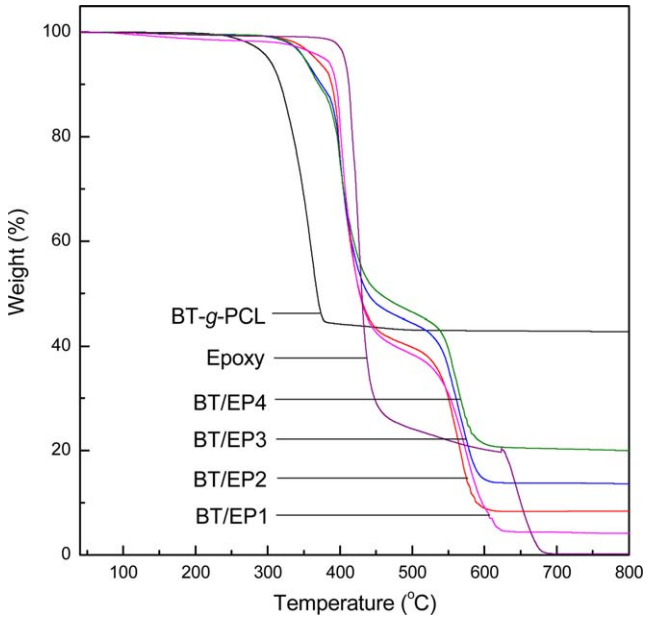

Figure 9. TGA curves of nanocomposites containing epoxy resins and different amounts of BT-*g*-PCL NPs. [Color figure can be viewed in the online issue, which is available at wileyonlinelibrary.com.]

good agreement with that of DSC, as shown in Figure 7. In addition, the intensity of the β relaxation also shifted to lower temperatures. The DMTA results further indicate that the PCL chains grafted onto the surface of the BT NPs were miscible with the epoxy matrices. The results of both DSC and DMTA indicated that the PCL chains grafted onto the surfaces of the BT NPs were miscible with the epoxy matrices. The miscibility of the PCL chains with epoxy networks was attributed to the formation of intermolecular hydrogen-bonding interactions between the carbonyl groups of the PCL chains and the hydroxyl groups of the epoxy networks.[51]

Thermal and Dielectric Properties

The thermal stability of the nanocomposites was investigated by means of TGA, and the TGA curves are presented in Figure 9. For comparison, the TGA curves of the control epoxy and BT-*g*-PCL NPs are also included. We observed that the organic–inorganic nanocomposites displayed TGA profiles similar to that of the control epoxy; this suggested that the incorporation of BT-*g*-PCL NPs did not significantly alter the degradation mechanism. The initial degradation of the nanocomposites appeared at about 350°C; this was slightly lower than that of control epoxy (405°C). The decreased initial degradation resulted from the PCL chains in the composites. In addition, the plateaus of degradation appeared after the temperatures at the maximum rate of degradation (ca. 450°C). It was proposed that the residues of decomposition at the degradation plateaus were composed of BT and the char from the epoxy thermosets. With increasing temperature to 800°C, the char from the epoxy thermosets disappeared under an air atmosphere, and thus, the residues of the nanocomposites resulted only from the inorganic BT NPs. The residues were detected to be 4.3, 8.4, 13.7, and 20.1% for BT/EP1, BT/EP2, BT/EP3, and BT/EP4, respectively; this was in good agreement with the incorporated content of BT NPs in the composites.

The dielectric properties of the nanocomposites containing epoxy and BT NPs were studied by broadband dielectric spectroscopy. Figure 10 shows the plots of the dielectric constants and losses as functions of the frequency of the applied electric fields in the range 10^3–10^6 Hz. For the control epoxy, the dielectric constants of the control epoxy were measured to be 5.24 and 4.09 at frequencies of 10^3 and 10^6 Hz, respectively, and the dielectric constant decreased with increasing frequency of the external electric field. This phenomenon showed that the establishment of effective polarization in the epoxy polymers did not shift quickly enough when the frequency of the applied electric field exceeded the relaxation frequency. When the BT-*g*-PCL NPs were incorporated into the epoxy, the dielectric constants of the nanocomposites were significantly enhanced, and the dielectric constants increased with increasing content of BT-*g*-PCL NPs. For the BT/EP4 nanocomposites, the dielectric constant increased up to 14.6 at a frequency of 10^3 Hz. Previous research work revealed that in the binary thermosetting blends of the epoxy with PCL, the dielectric constant did not significantly change in comparison with that of the control epoxy.[52] It was notable that the nanocomposites containing modified BT NPs (BT-*g*-PCL NPs) possessed higher dielectric constants than the composites containing plain BT NPs. For example, the BT/EP3 nanocomposites (where the content of BT NPs was 10 wt %) displayed a dielectric constant of 14.0, whereas the dielectric constant of the nanocomposites with the same content of BT NPs was reported to be about 7.2.[53] The increased dielectric constants of the nanocomposites were mainly attributed to the incorporation of BT NPs with high dielectric constants. It was proposed that there were two types of the major polarizations

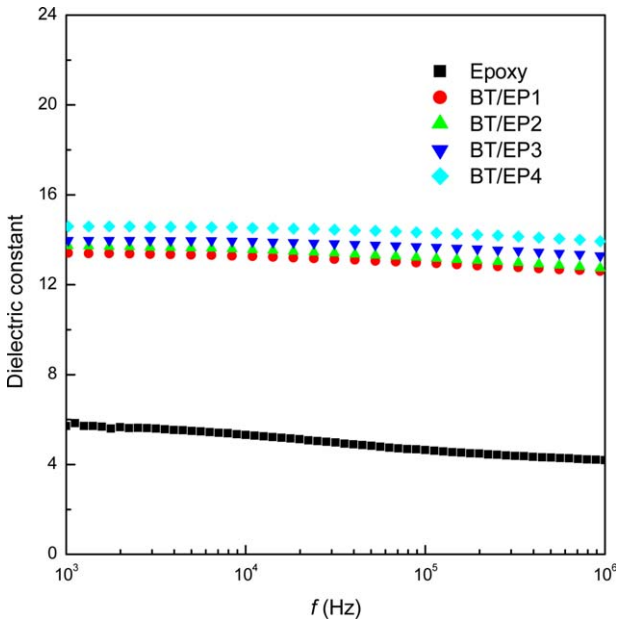

Figure 10. Plots of the dielectric constants of the control epoxy and the binary nanocomposites containing epoxy resins and different amounts of BT-*g*-PCL NPs at 25°C as a function of the ac frequency. [Color figure can be viewed in the online issue, which is available at wileyonlinelibrary.com.]

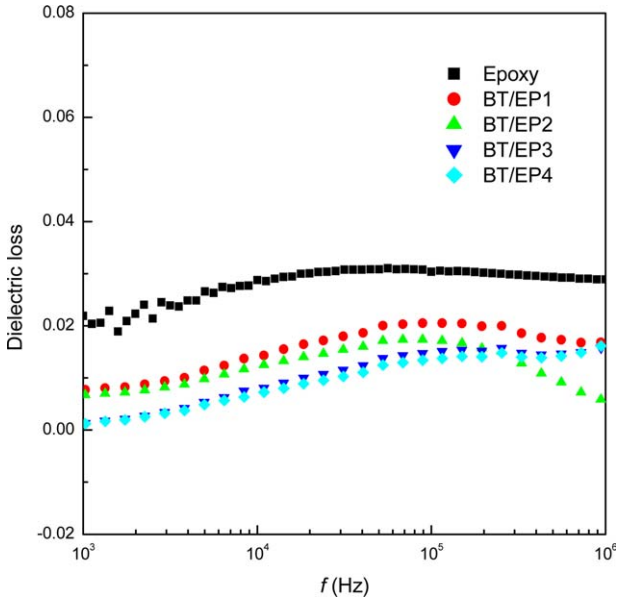

Figure 11. Plots of the dielectric loss tangent of the control epoxy and the binary nanocomposites containing epoxy resins and different amounts of BT-*g*-PCL NPs at 25°C as a function of the AC frequency (f). [Color figure can be viewed in the online issue, which is available at wileyonlinelibrary.com.]

in the nanocomposites: (1) dipolar polarization from all of the dipoles in the epoxy networks and (2) spontaneous polarization of the BT NPs. The former resulted from the polar bonds in the epoxy thermosets, whereas the latter resulted from the structural change where the center Ti^{4+} cations were displaced relative to the O^{2-} ions; this led to the formation of electric dipoles. In addition, the formation of BT nanophases in the epoxy matrix created a great interface between the epoxy matrix and BT nanophases; this resulted in considerable charge accumulation at the interface between the BT NPs and epoxy matrix under an external electrical field.[54,55] Therefore, interfacial polarization also significantly contributed the enhancement of dielectric constants.

The dielectric loss of the nanocomposites as the function of the frequency at room temperature is shown in Figure 11. In the control epoxy, the dielectric loss remained almost invariant (ca. 0.02), regardless of the alternating-current (ac) frequency. On the incorporation of BT NPs, the variation trend of the dielectric loss was similar to that of the control epoxy in a given range of frequency (10^3–10^6 Hz). In addition, the values of dielectric loss decreased significantly in comparison with that of the control epoxy. For the BT/EP4 nanocomposites, the dielectric constant decreased to 0.002 at a frequency of 10^3 Hz. The decrease in the dielectric loss could be understood with the following explanations:

1. The incorporation of PCL chains that were miscible with the epoxy matrix acted as the inert diluent of the dipoles in the epoxy thermosets. This decreased the dielectric loss of the nanocomposite system.
2. At this experimental temperature (i.e., room temperature), the crosslinked epoxy polymers were in a glass state. This suggested that the mobility of the molecular dipoles in the epoxy thermosets was not strong enough to cause the dissipation of the energy.
3. The fine dispersion of the BT NPs in the nanocomposites reduced the interfacial polarization relaxation between the BT NPs and the epoxy matrix. This significantly decreased the dielectric loss of the nanocomposites.

CONCLUSIONS

Through the use of PCL-grafted BT NPs, we successfully prepared nanocomposites involving epoxy and BT NPs via a physical blending approach. The results of both DSC and DMTA indicated that the PCL chains grafted onto the surfaces of the BT NPs were miscible with the epoxy matrices. The miscibility of the PCL chains with the epoxy networks improved the interfacial adhesion between the epoxy matrix and the BT NPs, which achieved a fine dispersion in the epoxy matrix. We found that the nanocomposites possessed excellent dielectric properties (i.e., a high dielectric constant and low dielectric loss). When the content of BT NPs was about 14 wt %, the dielectric constant of the nanocomposites was enhanced up to 14.6, whereas the dielectric loss still remained at quite a low level (i.e., 0.002 at a frequency of 10^3 Hz).

ACKNOWLEDGMENTS

The authors are grateful for the financial support of the Natural Science Foundation of China (contract grant number 51133003 and 21304058).

REFERENCES

1. Zheng, S In Epoxy Polymers: New Materials and Innovations; Pascault, J.-P., Williams, R. J. J., Eds.; Wiley-VCH: Weinheim, **2010**; p 79.
2. Ruiz-Pérez, L.; Royston, G. J.; Fairclough, J. P. A.; Ryan, A. J. *Polymer* **2008**, *49*, 4475.
3. Leonardi, A. B.; Fasce, L. A.; Zucchi, I. A.; Hoppe, C. E.; Soulé, E. R.; Pérez, C. J.; Williams, R. J. *Eur. Polym. J.* **2011**, *47*, 362.
4. Rousseau, I. A.; Xie, T. *J. Mater. Chem* **2010**, *20*, 3431.
5. Ulrich, R. K.; Schaper, L. W. Integrated Passive Component Technology; IEEE: Hoboken, NJ, **2003**.
6. Prymark, J.; Bhattacharya, S.; Paik, K.; Tummala, R. R. Fundamentals of Microsystems Packaging; McGraw-Hill: New York, **2001**.
7. Sharma, R. A.; D'Melo, D.; Bhattacharya, S.; Chaudhari, L.; Swain, S. *IEEE Trans. Dielectr. Electr. Insul.* **2012**, *13*, 31.
8. Wang, Z.; Nelson, J. K.; Hillborg, H.; Zhao, S.; Schadler, L. S. *Adv. Mater.* **2012**, *24*, 3134.
9. Yu, A. P.; Ramesh, P.; Itkis, M. E.; Bekyarova, E.; Haddon, R. C. *J. Phys. Chem. C* **2007**, *111*, 7565.
10. Bai, Y.; Cheng, Z.; Bharti, V.; Xu, H.; Zhang, M. Q. *Appl. Phys. Lett.* **2000**, *76*, 3804.
11. Zhang, Q.; Li, H.; Poh, M.; Xia, F.; Cheng, Z.; Xu, H.; Huang, C. *Nature* **2002**, *419*, 284.
12. Qi, L.; Lee, B.; Chen, S.; Samuels, W.; Exarhos, G. *Adv. Mater.* **2005**, *17*, 1777.
13. Arbatti, M.; Shan, X.; Cheng, Z. *Adv. Mater.* **2007**, *19*, 1369.

14. Guo, N.; DiBenedetto, S.; Kwon, D.; Wang, L.; Russell, M.; Lanagan, M.; Facchetti, A.; Marks, T. *J. Am. Chem. Soc.* **2007**, *129*, 766.
15. Xu, H.; Dang, Z.; Jiang, M.; Yao, S.; Bai, J. *J. Mater. Chem.* **2008**, *18*, 229.
16. Yao, J.; Xiong, C.; Dong, L.; Lei, Y.; Chen, L.; Li, R.; Zhu, Q.; Liu, X. *J. Mater. Chem.* **2009**, *19*, 2817.
17. Kim, P.; Doss, N.; Tillotson, J.; Hotchkiss, P.; Pan, M.; Marder, S.; Li, J.; Calame, J.; Perry, J. *ACS Nano* **2009**, *3*, 2581.
18. Yuan, J.; Dang, Z.; Yao, S.; Zha, J.; Zhou, T.; Li, S.; Bai, J. *J. Mater. Chem.* **2010**, *20*, 2441.
19. Dang, Z. M.; Wang, L.; Yin, Y.; Zhang, Q.; Lei, Q. Q. *Adv. Mater.* **2007**, *19*, 852.
20. Wang, C. C.; Song, J. F.; Bao, H. M.; Shen, Q. D.; Yang, C. Z. *Adv. Funct. Mater.* **2008**, *18*, 1299.
21. Zhang, J.; Mine, M.; Zhu, D.; Matsuo, M. *Carbon* **2009**, *47*, 1311.
22. Li, Y.; Pothukuchi, S.; Wong, C. P. Proceedings of the 54th IEEE Electronic Components and Technology Conference; Las Vegas, NV, **2004**; p 507.
23. Psarras, G. C.; Manolakaki, E.; Tsangaris, G. M. *Compos. A* **2002**, *33*, 375.
24. Lu, J.; Moon, K. S.; Kim, B. K.; Wong, C. P. *Polymer* **2007**, *48*, 1510.
25. Wang, J. W.; Wang, Y.; Wang, F.; Li, S. Q.; Xiao, J.; Shen, Q. D. *Polymer* **2009**, *50*, 679.
26. Li, Z.; Fredin, L.; Tewari, P.; DiBenedetto, S.; Lanagan, A.; Ratner, M.; Marks, T. *Chem. Mater.* **2010**, *22*, 5154.
27. Yang, T.; Kofinas, P. *Polymer* **2007**, *48*, 791.
28. Li, J.; Seok, S.; Chu, B.; Dogan, F.; Zhang, Q.; Wang, Q. *Adv. Mater.* **2009**, *21*, 217.
29. Balasubramanian, B.; Kraemer, K.; Reding, N.; Skomski, R.; Ducharme, S.; Sellmyer, D. *ACS Nano* **2010**, *4*, 1893.
30. Barber, P.; Pellechia, P.; Ploehn, H.; Zur Loye, H. *ACS Appl. Mater. Interfaces* **2010**, *2*, 2553.
31. Alam, M. A.; Azarian, M. H.; Pecht, M. G. *J. Electron. Mater.* **2013**, *42*, 1101.
32. Windlass, H.; Raj, P. M.; Balaraman, D.; Bhattacharya, S. K.; Tummala, R. R. *IEEE Trans. Electron. Packag. Manuf.* **2003**, *26*, 100.
33. Iijima, M.; Sato, N.; Wuled Lenggoro, I.; Kamiya, H. *Colloids Surf. A* **2009**, *352*, 88.
34. Luo, S.; Yu, S.; Sun, R.; Liang, X.; Lai, M. In Proceedings of 2012 International Conference on Electronic Packaging Technology & High Density Packaging, Guilin, China, **2012**; p 457.
35. Saidina, D. S.; Mariatti, M.; Julie, M. J. *J. Mater. Sci. Mater. Electron.* **2014**, *25*, 4923.
36. Hyun, J. G.; Paik, K. W.; Pak, J. S. In Characterization of Epoxy/$BaTiO_3$ Composite Embedded Capacitors for High Frequency Behaviors, 59th Electronic Components and Technology Conference; ECTC 2009: San Diego, CA, **2009**; p 2046.
37. Huang, X.; Xie, L.; Yang, K.; Wu, C.; Jiang, P.; Li, S.; Wu, S.; Tatsumi, K.; Tanaka, T. R. *IEEE Trans. Dielectr. Electr. Insul.* **2014**, *21*, 480.
38. Chao, F.; Liang, G.; Kong, W.; Zhang, Z.; Wang, J. *Polym. Bull.* **2008**, *60*, 129.
39. Huang, X.; Xie, L.; Yang, K.; Wu, C.; Jiang, P.; Li, S.; Wu, S.; Tatsumi, K.; Tanaka, T. *IEEE Trans. Dielectr. Electr. Insul.* **2014**, *21*, 467.
40. Jackson, W.; Reddish, W. *Nature* **1945**, *156*, 717.
41. Mitsui, T.; Westphal, W. B. *Phys. Rev.* **1961**, *124*, 1354.
42. Yin, M.; Zheng, S. *Macromol. Chem. Phys.* **2005**, *206*, 929.
43. Ni, Y.; Zheng, S. *Polymer* **2005**, *46*, 5828.
44. Xie, L.; Huang, X.; Huang, Y.; Yang, K.; Jiang, P. *ACS Appl. Mater. Interfaces* **2013**, *5*, 1747.
45. Requena, S.; Lacoul, S.; Strzhemechny, Y. M. *Materials* **2014**, *7*, 471.
46. Lopez, M.; Fourlaris, G.; Rand, B.; Riley, F L. *J. Am. Ceram. Soc.* **1999**, *82*, 1777.
47. Kamel, F.; Gonon, P.; Jomni, F.; Yangui, B. *J. Eur. Ceram. Soc.* **2007**, *27*, 3807.
48. Tang, H.; Zhou, Z.; Sodano, H. *ACS Appl. Mater. Interfaces* **2014**, *6*, 5450.
49. Nojima, S.; Hashizume, K.; Rohadi, A.; Sasaki, S. *Polymer* **1997**, *38*, 2711.
50. Jones, A. A. *Macromolecules* **1985**, *18*, 902.
51. Zhang, C.; Li, L.; Zheng, S. *Macromolecules* **2013**, *46*, 2740.
52. Li, J.; Cong, H.; Li, L.; Zheng, S. *Polymer* **2015**, *69*, 193.
53. Sangermano, M.; Lombardi, M.; Guerriero, A.; Kortaberria, G.; Mondragon, I.; Pirri, F.; Montanaro, L. *Macromol. Mater. Eng.* **2013**, *298*, 634.
54. Wagner, K. W. *Arch. Elektrotech.* **1914**, *2*, 371.
55. Sillars, R. W. J. *Inst. Electr. Eng.* **1937**, *80*, 378.